

## ARTICLE OPEN



# 270 nm ultra-thin self-adhesive conformable and long-term air-stable complimentary organic transistors and amplifiers

Mohammad Javad Mirshojaeian Hosseini<sup>1</sup>, Yi Yang <sup>1</sup>, Walter Kruger <sup>1</sup>, Tomoyuki Yokota <sup>2</sup>, Sunghoon Lee<sup>2</sup>, Takao Someya <sup>2</sup> and Robert A. Nawrocki <sup>1</sup>✉

Lightweight, flexible, and conformal bioelectronics are essential for wearable technologies. This paper introduces 270 nm thin organic electronics amplifying circuits that are self-adhesive, skin conformal, and long-term air-stable. This report studies the effect of total device thickness, namely 3  $\mu\text{m}$  and 270 nm devices, on the characterization of organic devices before and after buckling, the longevity of organic field-effect transistors (OFETs) over 5 years, and the lamination of OFETs on the human skin. A single-stage organic complementary inverter and a pseudo-complementary amplifier are fabricated to compare their electrical characteristics, with amplification gains of 10 and 64, respectively. Finally, the study demonstrates a five-stage organic complementary inverter can successfully amplify artificial electromyogram and electrocardiogram signals with gains of 1000 and 1088, respectively.

*npj Flexible Electronics* (2023)7:38; <https://doi.org/10.1038/s41528-023-00267-y>

## INTRODUCTION

Wearable health monitoring systems are expected to play an increasingly more integral role in the future of medical devices<sup>1</sup>. At present, commercially available wearable devices are rigid and non-conformal resulting in unreliable collected data. However, on-skin laminated ultra-thin and conformal bioelectronics will enable sensors to extract very weak electronic biopotentials, in the range of mV, amplify them as close to the source as possible, and provide ultra-sensitivity without any crosstalk or interference noise<sup>2,3</sup>. A thinner film is more conformal without any nanostructures or an additional adhesive, and results in improved signal fidelity, such as lower noise or motion artifacts<sup>4</sup>. Over time, laminated bioelectronics have produced complex applications, such as chemical<sup>5,6</sup>, physical<sup>7</sup>, electromyogram (EMG), and electrocardiogram (ECG) sensors<sup>8,9</sup>.

While the majority of applications rely on silicon-based electronics, organic electronics are gaining popularity due to their characteristics including lightweight, physical flexibility, ultra-thinness, low-cost fabrication, and large-area fabrication<sup>10–14</sup>. Many examples of organic electronics in biomedical applications have been demonstrated<sup>15</sup>, such as low voltage biosensors<sup>16</sup>, DNA hybridization detection<sup>17</sup>, and in vivo recording of brain activities<sup>18</sup>. Ultra-thin organic networks and devices redefine how body measurements are taken and provide a steady influx of information about their general health conditions in in-vitro and in-vivo environments<sup>19</sup>.

Organic field effect transistors (OFETs) are the basic blocks in electrical structures and have been demonstrated in various healthcare applications<sup>20,21</sup>. Within this scope, organic amplifiers that comprise complimentary OFETs are promising candidates to accomplish real-time recording and amplify weak ( $\mu\text{V}$ ) signals close to the site of interest<sup>22</sup>. The advances in organic device fabrication have broadened the utilization of organic amplifiers in laminated film applications such as biosignal acquisition<sup>23,24</sup>. However, the nature of organic materials introduces challenges including stability, reliability, and device-to-device variability.

Some of these challenges have been addressed, but most remained unsolved<sup>25</sup>.

Here, we demonstrate the viability of 270 nm organic complementary organic transistors, showcasing their ability to amplify weak biological signals, their physical flexibility, and their long-term air stability of over 5 years. Based on our previously demonstrated 270 nm electronic skin (e-skin) fit with organic transistors and sensors<sup>26,27</sup>, the fabrication of  $\sim$ 270 nm thin, lightweight, conformal, self-adhesive e-skin, fit with p and nOFETs, that can adhere to human skin and measure biological signals has been demonstrated. We provide simulations of the prepared devices and circuits as a means to reduce the cost of device preparation and validate the results of experimental characterization. The fabrication, simulation, and characterization of individual p and nOFETs are described. The effect of buckling and lamination of OFETs on human skin is also studied. To show the long-term air stability, the characterization of p and nOFETs fabricated 5 years prior are demonstrated over time. Organic complementary metal oxide semiconductor (oCMOS) inverter, organic pseudo-CMOS inverter (opCMOS), and organic Ring Oscillator (oRO), from 270 nm technology, are fabricated, characterized, and simulated. The oRO is modified to form a five-stage oCMOS inverter and has shown amplifying artificial ECG and EMG signals. Characterization of these measurements provides insight into the expected gain levels, performance values, and applicability of organic devices fabricated to serve as biosensors for medical and biomedical areas of study.

## RESULTS

### Fabrication

The OFETs and circuits are fabricated according to previously published research about 270 nm organic transistors and biopotential electrodes<sup>26,27</sup>. In brief, 30 nm of gold (Au) is thermally deposited and sandwiched between two 60 nm layers of Parylene diX-SR. The organic semiconducting layers, dinaphtho [2,3-b:2',3'-f] thieno[3,2-b]thiophene (DNNT) for p-type OFETs (pOFETs)<sup>28</sup>, and

<sup>1</sup>School of Engineering Technology, Purdue University, 401 S Grant St, West Lafayette, IN 47906, USA. <sup>2</sup>Department of Electrical Engineering and Information Systems, School of Engineering, The University of Tokyo, 7-3-1 Hongo Bunkyo-ku, Tokyo 113-8656, Japan. ✉email: robertnawrocki@purdue.edu

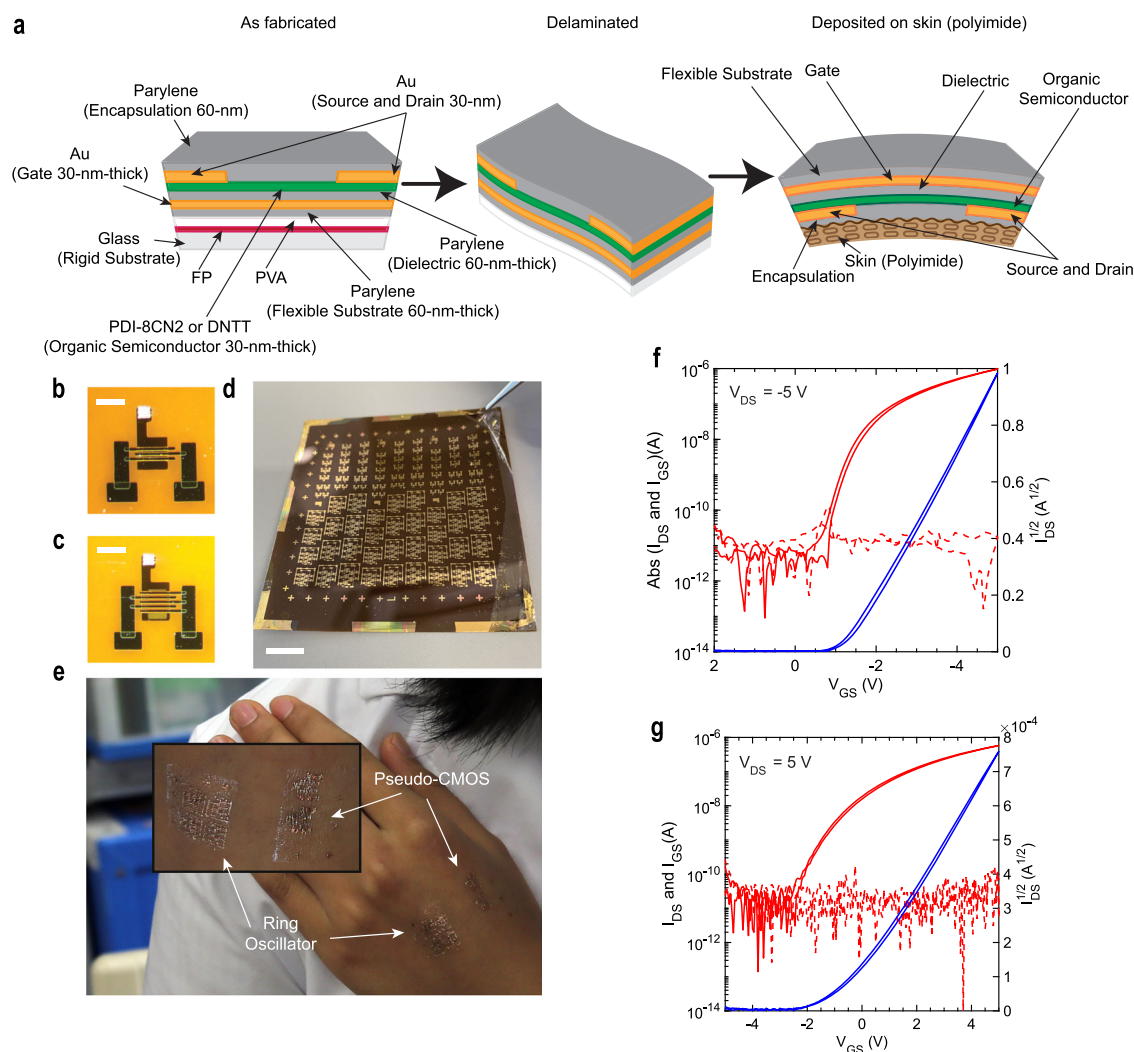


**Fig. 1** The OFETs structure, photos, and characterization results. **a** The device structure and fabrication process of OFETs with photographs of **b** the nOFET (scale bar, 500  $\mu\text{m}$ ), **c** the pOFET (scale bar, 500  $\mu\text{m}$ ), the laminated device on **d** a polyimide film (scale bar, 10 mm), and **e** human skin. The characteristic curves of the 270 nm **f** pOFET and **g** nOFET.

N,N'-bis(n-octyl),1,6-dicyanoperylene-3,4:9,10-bis(dicarboximide) (PDI-8CN2, sometimes also referred to as N1200) for n-type OFETs (nOFETs)<sup>29</sup> are thermally deposited on Parylene. Following the organic active layer deposition, 30 nm of Au is deposited as the source, gate, and circuit interconnect, and encapsulated by a 60 nm thin layer of Parylene for a total structure thickness of  $\sim 270$  nm, with via holes obtained via laser ablation. The layers are deposited sequentially on a 1 mm-thick glass substrate during the fabrication process. Fluorinated polymer (FP;  $\sim 85$  nm) plays the role of releasing layer, and the polyvinyl alcohol (PVA;  $\sim 5$   $\mu\text{m}$ ) layer facilitates the handling of the film after delamination from glass. The film is delaminated manually from the glass substrate and gently placed on a stretched skin upside down. The process is finished by removing the PVA layer using  $\text{H}_2\text{O}$  spray. During the experiments, the film is laminated on a 125  $\mu\text{m}$ -thick polyimide (PI) film to expedite the circuit characterization process. The fabrication process and device stacks are shown in Fig. 1a.

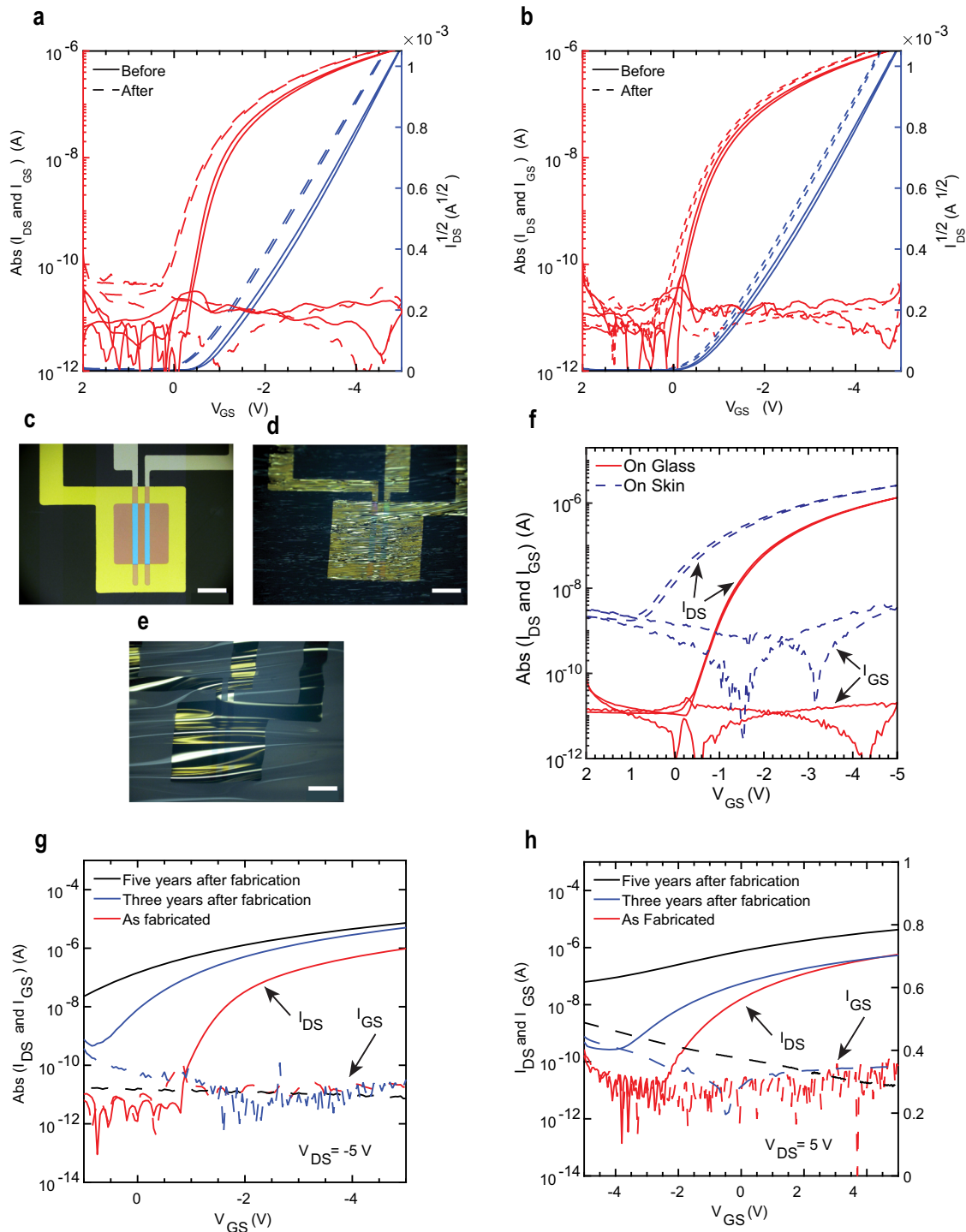
### Characterization

Figure 1b–d shows the single pOFET and nOFETs, and the laminated chip on a PI film, respectively. The pOFET has a channel length of 30  $\mu\text{m}$  and a channel width of 800  $\mu\text{m}$ , and the nOFET has the same channel length and width of 3200  $\mu\text{m}$  (to account for lower carrier mobility compared with pOFET). Also, the

opCMOS and oRO are laminated directly on the human skin, as shown in Fig. 1e, with no additional adhesives. Using HP 4145A semiconductor parameter analyzer (SPA), both types of OFETs are characterized by plotting their output and transconductance curves. Figure 1f and g demonstrate the measured characteristics of p and nOFETs. Considering the disparity in channel widths, the mobility and threshold voltages of p and nOFETs are 0.11, 0.007  $\text{cm}^2 \text{V}^{-1} \text{s}^{-1}$ , and  $-1.23$ ,  $-0.77$  V, respectively. The lower mobility, larger threshold voltage, and higher OFF current of nOFET compared to pOFET are intrinsic characteristics of organic n-type semiconductors that are mainly due to the incompatibility of the gold electrodes' work function and the n-type semiconductors' lowest unoccupied molecular orbital (LUMO) level<sup>30,31</sup>. Supplementary Figure 1a–f demonstrates the characterization results of seven p and nOFETs to show device-to-device variability. Supplementary Tables 1 and 2 summarized the statistical data regarding Supplementary Fig. 1a–f.

### Flexibility

The physical flexibility of OFETs is an essential quality in biomedical instrumentation and wearable device applications. The thinner OFETs increase the overall flexibility and enable the device to buckle when placed on a bendable and stretchable surface such as skin<sup>32,33</sup>. Figure 2a and b demonstrate the



**Fig. 2** Buckling test results and the OFETs characterization results over 5 years. **a** Transconductance curves of 270 nm and **b** 3  $\mu\text{m}$ -thick pOFETs, before and after buckling tests. Photographs of pOFET film **c** before and **d** after buckling, comparing **e** buckled 3  $\mu\text{m}$  film. Scale bars are 400  $\mu\text{m}$ . **f** The comparison of characteristic curves of 270 nm pOFET on the glass substrate and laminated on human skin. The comparison of transconductance curves of 270 nm thick **g** p and **h** nOFETs extracted as fabricated, three, and 5 years after fabrication.

transconductance curves for a 270 nm and 3  $\mu\text{m}$ -thick pOFET before and after buckling, respectively. The study shows the effect of substrate thickness on the characteristics of a laminated single pOFET. The 3  $\mu\text{m}$  device comprises a 270 nm-thick pOFET laminated on a 3  $\mu\text{m}$ -thick substrate.

Figure 2a and b show similar results. The ON and OFF currents of 1  $\mu\text{A}$  and 10 pA when  $V_{GS} = -5$  V and  $V_{GS} = 0$  V, respectively. Also, buckling shifts  $I_{DS}$  to a higher value and the threshold

voltage to a smaller one, but the leakage current remains unchanged. Otherwise, the performance of the OFETs is independent of their thicknesses. Figure 2c to e shows the photographs of 270 nm OFET before and after buckling compared to 3  $\mu\text{m}$  OFET after buckling, respectively.

Figure 2f demonstrates the characterization results in transconductance curves when a 270 nm pOFET on glass (before delamination), versus one of the most applicable soft materials:

human skin. Immediately after lamination on the skin, the OFF current increases from  $10^{-11}$  A for glass, to  $10^{-9}$  A on the skin, which is correspondent for an increase of the leakage current. This is likely due to the diffusion of ionic sweat into the conducting channel, which is only separated from the skin by the ultra-thin (60 nm) layer of encapsulating Parylene. Supplementary Figure 2 shows the device characterization after delamination from the glass substrate and after lamination with the PVA layer on the skin to prove the claim as mentioned earlier. Additionally, the shift of the ON current and the threshold voltage are likely the result of the film being repeatedly bent with nano-delamination of individual layers of the OFET causing charges to be trapped in between.

### Stability

Stability is one of the main properties of healthcare devices; for instance, a pacemaker that stimulates a heart has a lifetime of 10 years. At present, however, organic electronic devices are not as stable as inorganic electronics and degrade when exposed to external environmental factors, for instance, moisture and oxygen<sup>34</sup>. The  $\pi$ -conjugated active layers are susceptible to degradation in organic electronic devices, while inorganic semiconductors are mostly intrinsically stable<sup>35</sup>. The degradation is a complicated process, and the factors such as light<sup>36</sup>, heat<sup>37</sup>, chemicals<sup>38</sup>, water<sup>39</sup>, and oxygen<sup>40</sup>, all accelerate it. Barrier films sometimes referred to as encapsulation layers, are a conventional method to protect the active layer against ambient factors and impede degradation<sup>38</sup>. The barrier architectures vary based on organic device fabrication methods<sup>35</sup>. As the diffusion process is relatively linear, thicker layers afford longer protection. Inorganic capsulation materials are more common due to longer oxygen and water permeation compared to polymer barriers<sup>41,42</sup>.

This study presents organic electronic devices encapsulated using an ultra-thin layer of polymer, a 60 nm-thick Parylene that guarantees a pinhole-free film<sup>43</sup>. Figure 2g and h compare the p and nOFETs' transconductance curves as fabricated, 3 and 5 years after fabrication, respectively. The devices have been stored in ambient conditions and annealed three times for 1 h at 120 °C during the period in a glovebox filled with nitrogen. The post-deposition annealing of OFETs enhances the mobility and morphology of active layers and releases oxygen and moisture that were trapped/infused in active/encapsulation layers<sup>44,45</sup>. The mobilities of p and nOFETs have decreased; however, the threshold voltages have increased over time, likely resulting from the accumulation of oxygen and moisture in the Parylene layer. Also, the ON and OFF currents have shifted to higher values, resulting from the penetration of environmental factors (mainly oxygen and moisture) into the active layer and preventing the device from turning off<sup>39,40</sup>. This comparison provides insight into the air stability of the OFETs over the lifetime which is paramount for the practical use of OFETs in biomedical devices and open-air networks, where the longevity of the OFET itself is just as valued as the data it can provide.

### Amplifiers

Biological signals are weak, on the order of microvolts to millivolts, and need to be processed (such as amplified and filtered). However, the signals need to be transferred because the processing components are located away from the source, consequently exposing the signals to noise artifacts<sup>46</sup>. Hence, ultra-thin organic amplifiers can provide direct amplification near the site and suppress the effects of transmission noise<sup>47–49</sup>. Three amplifying circuits have been studied vastly: opCMOS, multi-stage oCMOS, and differential amplifiers. These amplifiers operate at a low voltage and exhibit high gains than the other ultra-thin organic amplifiers<sup>47,50–53</sup>. The opCMOS amplifier relies on only pOFETs which greatly simplifies the fabrication, compared to the

other circuits composed of complimentary OFETs. Differential amplifiers are capable of suppressing common-mode noise while amplifying weak signals<sup>52</sup>. However, noise elimination is out of the scope of this study, and two other types of amplifiers are fabricated and characterized. The opCMOS and a single-stage oCMOS are fabricated using the technology discussed in the section "Fabrication". Figure 3a shows the schematic of an opCMOS circuit composed of only pOFETs that offer higher mobility and less mismatch effect than nOFETs<sup>54</sup>. Figure 3b and c demonstrate the opCMOS amplifier before and after lamination on top of a 3  $\mu$ m-thick film (a thicker substrate makes the handling easier while the electrical characteristics remain the same, as shown in the previous section), respectively, to study the effect of buckling on the circuit performance. Figure 3d presents the characterization results of the circuit before and after buckling for  $V_{DD}$ s ranging from 2 to 5 V using solid and dashed lines, respectively. Table 1 shows that the gain reaches 64.57 for 5 V while the switching voltage exceeds the  $V_{DD}$  values which makes opCMOS less effective in bio-signal amplification. Besides, buckling decreases the gain and increases the switching voltage. The amplitude and wavelength of buckled films were previously estimated to be approximately 246 and 305  $\mu$ m for 3  $\mu$ m films, and 3.4 and 17.4  $\mu$ m for 300 nm films<sup>27</sup>.

Organic CMOS inverters offer a low switching voltage that addresses the high operating voltage of opCMOS. Figure 3e shows the oCMOS schematic circuit, and Fig. 3f depicts the circuit before and after lamination on a 3  $\mu$ m-thick substrate. Figure 3h and Table 2 demonstrate the gain discrepancy is in the range of <1 V before and after buckling while the switching voltage decreases. The oCMOS has a lower gain compared to opCMOS with the same  $V_{DD}$ s, but operating (switching) voltages are about half, and the effect of buckling is neglectable (<1 V for the gain and about 1 V for the switching voltage), which are closer to the needs of healthcare applications. A multi-stage oCMOS addresses the gain issue; however, it increases the complexity of the circuit. Supplementary Fig. 1g–l demonstrates the characterization results of seven opCMOS and oCMOS amplifiers to show device-to-device variability. Supplementary Tables 3 and 4 summarized the statistical data regarding Supplementary Fig. 1g–l.

Figure 4a–c shows the circuit schematic, a photograph, and characterization result of an oRO based on five-stage oCMOS inverters, with an odd number of inverters where the input of the next stage inverter is connected to the output of a previous stage inverter. The oRO circuit is fabricated and then modified to form a five-stage oCMOS. Figure 4d–h depicts the characterization results for one- to five-stage oCMOS, respectively. The results indicate a presence of hysteresis, with a modest difference in magnitude of gain and the switching voltage dependent on the sweep direction of  $V_{IN}$ <sup>11</sup>. Table 3 shows the maximum gains and switching voltages in forwarding and backward  $V_{IN}$ 's directions. Also, the gain in a multi-stage oCMOS is theoretically a factor of the single-stage gain; however, the mismatch between OFETs' characteristics keeps the gain lower than expected. The maximum gain of a five-stage oCMOS exceeds 2358 in the backward direction while the  $V_{DD}$  is 8 V and the switching voltage is swinging around 5 V.

### Simulation

The electrical characteristics of complex analog circuits can be predicted or verified by means of circuit simulation. To date, the simulation software with integrated circuit emphasis (SPICE, or "Simulation Program with Integrated Circuit Emphasis") technology, which is based on modeling the electrophysical characteristics of modular electronic components, has been well established and has played an important role in the design and optimization of very large-scale integrated circuits<sup>55,56</sup>. However, SPICE simulation of organic analog circuits still faces great challenges since the physical characteristics of OFETs are



substantially different from those of conventional silicon-based transistors. It should be noted that compared to the simulation of analog devices composed of silicon-based metal-oxide-semiconductor field-effect-transistors, the simulation of organic analog circuits with OFETs remains an open research topic and

requires more innovative approaches due to the disordered crystal structure of organic semiconductors, the physical flexibility of thin-film OFETs and the variability of OFETs in the same analog circuit<sup>57–59</sup>. With this in mind, our study is not seeking a very precise match between the simulation results and our experi-

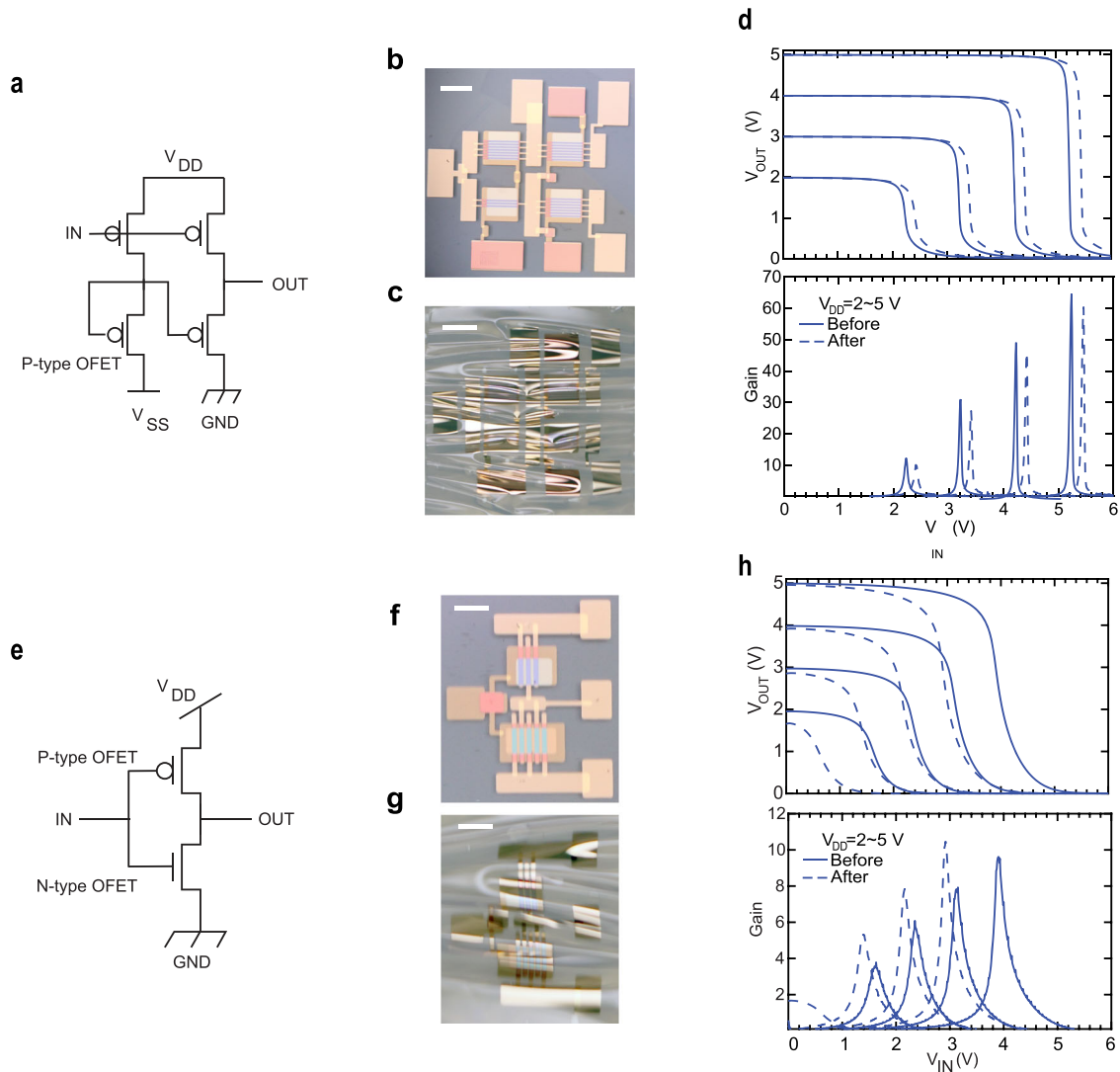


**Fig. 3** The organic CMOS and organic pseudo-CMOS inverters characterization results. **a** The schematic circuit of the opCMOS inverter. Images of the opCMOS inverter in **b** flat, before crumpling, and **c** buckled states. Scale bars are 1 mm. **d** Characteristic curves of the 270 nm-thick opCMOS inverter before and after buckling. **e** The schematic circuit of the single-stage oCMOS inverter. Images of the single-stage oCMOS inverter in **f** flat, before crumpling, and **g** buckled states. Scale bars are 500  $\mu\text{m}$ . **h** Characteristic curves of the 270 nm-thick single-stage oCMOS inverter before and after buckling.

**Table 1.** The gains and switching voltages of the opCMOS inverter before and after buckling are shown in Fig. 3b and c.

$V_{DD}$ (V)	Before buckling		After buckling	
	Gain	$V_{Swch}^a$ (V)	Gain	$V_{Swch}$ (V)
5	64.57	5.24	60.32	5.46
4	49.97	4.23	45.92	4.42
3	30.97	3.22	27.26	3.41
2	12.20	2.22	10.06	2.40

<sup>a</sup>Switching voltage.

**Table 2.** The gains and switching voltages of the oCMOS before and after buckling are shown in Fig. 3f and g.

$V_{DD}$ (V)	Before buckling		After buckling	
	Gain	$V_{Swch}^a$ (V)	Gain	$V_{Swch}$ (V)
5	9.61	3.9	10.47	2.92
4	7.92	3.15	7.85	2.16
3	6.08	2.35	5.33	1.39
2	3.78	1.63	2.90	0.63

<sup>a</sup>Switching voltage.

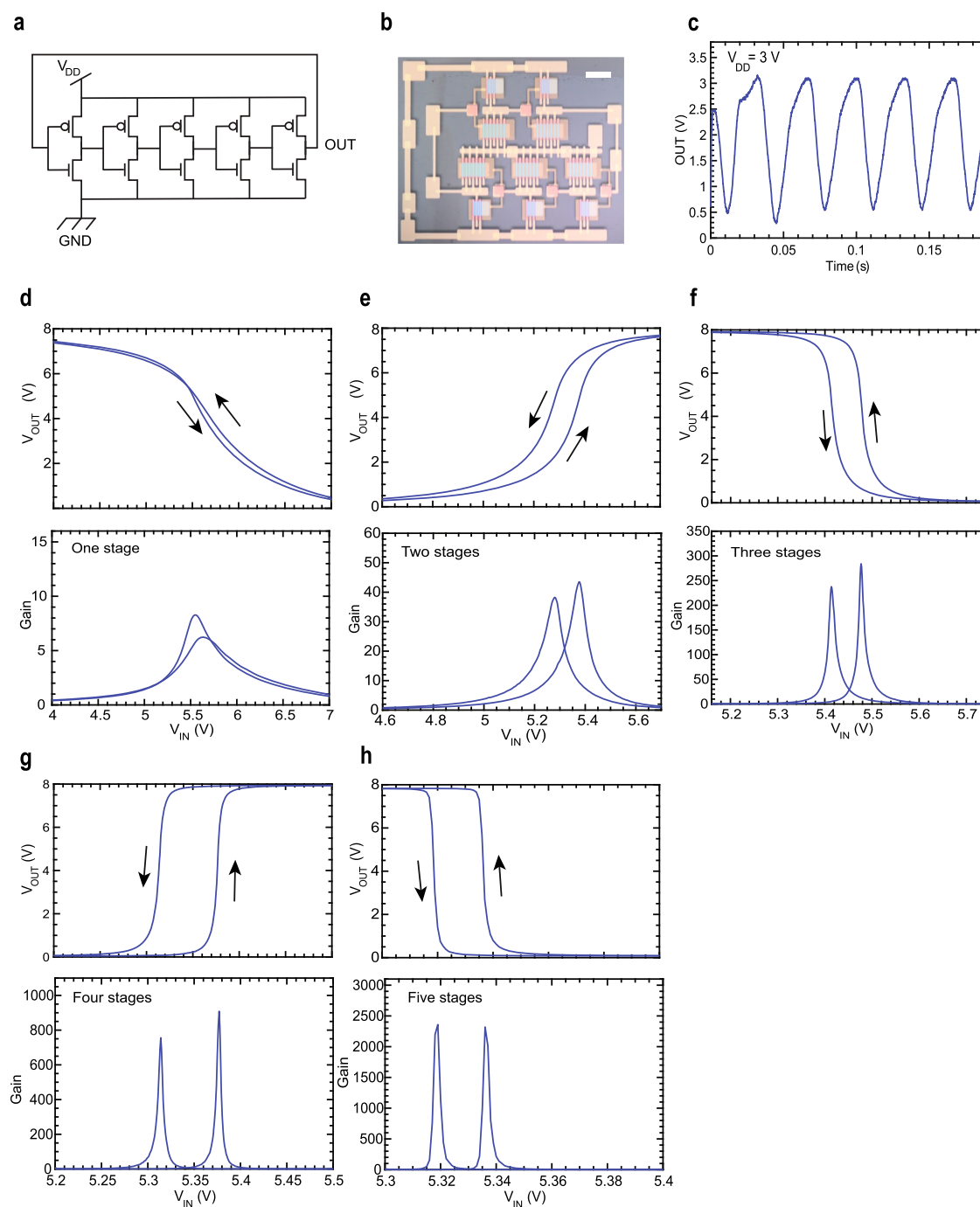


**Fig. 4** The organic ring oscillator test results. **a** The circuit schematic, **b** the image, and **c** the output characteristics of the oRO. Scale bar, 500  $\mu\text{m}$ . Transfer characteristic functions and gains of the **d** one-, **e** two-, **f** three- **g** four-, and **h** five-stage organic CMOS inverter.

mental measurements, but it can validate our organic analog circuits to some extent and inspire the design and preparation of the circuits. In this paper, in addition to the design and fabrication of oCMOS circuits, our customized SPICE-level OFET model is employed to simulate and verify the measured input and output characteristics of the prepared organic devices and circuits.

To address the above-mentioned discrepancies, our model utilizes Marinov's approach to describe the above-threshold transconductance of OFETs and takes into account the metal–insulator–semiconductor (MIS) tunneling current in the subthreshold regime<sup>60,61</sup>. The MIS tunneling current, which is modeled as a double-exponential function of the gate voltage,

arises from the tunneling effect of minority carriers at the semiconductor–insulator interface and was reported to be the main source of subthreshold currents in devices with thin insulating layers, such as MIS tunnel diodes and Gated-MIS tunnel transistors<sup>62,63</sup>. In Fig. 5a and b, the simulated transconductance (red symbols) and experimentally measured transconductance (blue curves) for the p and nOFETs are demonstrated. A good agreement between the measured and simulated transconductance can be seen for both the p and nOFETs in their whole  $V_{GS}$  regions. This observation suggests that our OFET model with tuned parameters reflects the true transconductance of the real OFETs. It is then possible to simulate the overall circuit responses

**Table 3.** The gains and switching voltages of the multi-stage oCMOS are shown in Fig. 4d–h.

	Forward		Backward	
	Gain	$V_{Sw}^a$ (V)	Gain	$V_{Sw}$ (V)
1 stage	8.28	5.56	6.23	5.63
2 stages	43.04	5.38	38.12	5.28
3 stages	271.96	5.48	232.24	5.41
4 stages	729.72	5.38	622.27	5.31
5 stages	2319.48	5.34	2358.92	5.32

<sup>a</sup>Switching voltage.

of the organic integrated circuits because the individual OFETs are taken as basic modules in our circuits. Figure 5c–j shows the simulated and measured responses of our fabricated poCMOS, oCMOS amplifiers, and ring oscillator. It can be observed that the experimentally measured circuit responses are similar to the simulated results, which is not only reflected in the similar shape of the transfer curves but also in the comparable gains of oCMOS amplifiers. This finding implies the correctness of the dynamic responses of the circuits that were characterized in our experiments and further confirms the soundness of the design and manufacturing process of our organic devices. However, it should be noted that an exception appears in Fig. 5d, where some discrepancy occurs between our simulation results and experimental measurements. This is because the measured data for a single-stage oCMOS with  $V_{DD} = 5$  V in Fig. 5f and d are inherently different. Since the same set of model parameters was used to simulate the single-stage oCMOS, the simulation results can only match the experimental data of one of the two figures. The measurement discrepancy can be attributed to the individual variability of the OFETs in the different oCMOS devices and to the residual stress inside the ultra-thin devices during the measurement<sup>64,65</sup>. Moreover, the physical flexibility of the measurement process affecting the electrical characteristics (e.g., threshold voltage, carrier mobility) of OFETs can be another reason why different switching voltages are obtained for the same oCMOS amplifier in different measurement trials<sup>60,66–68</sup>.

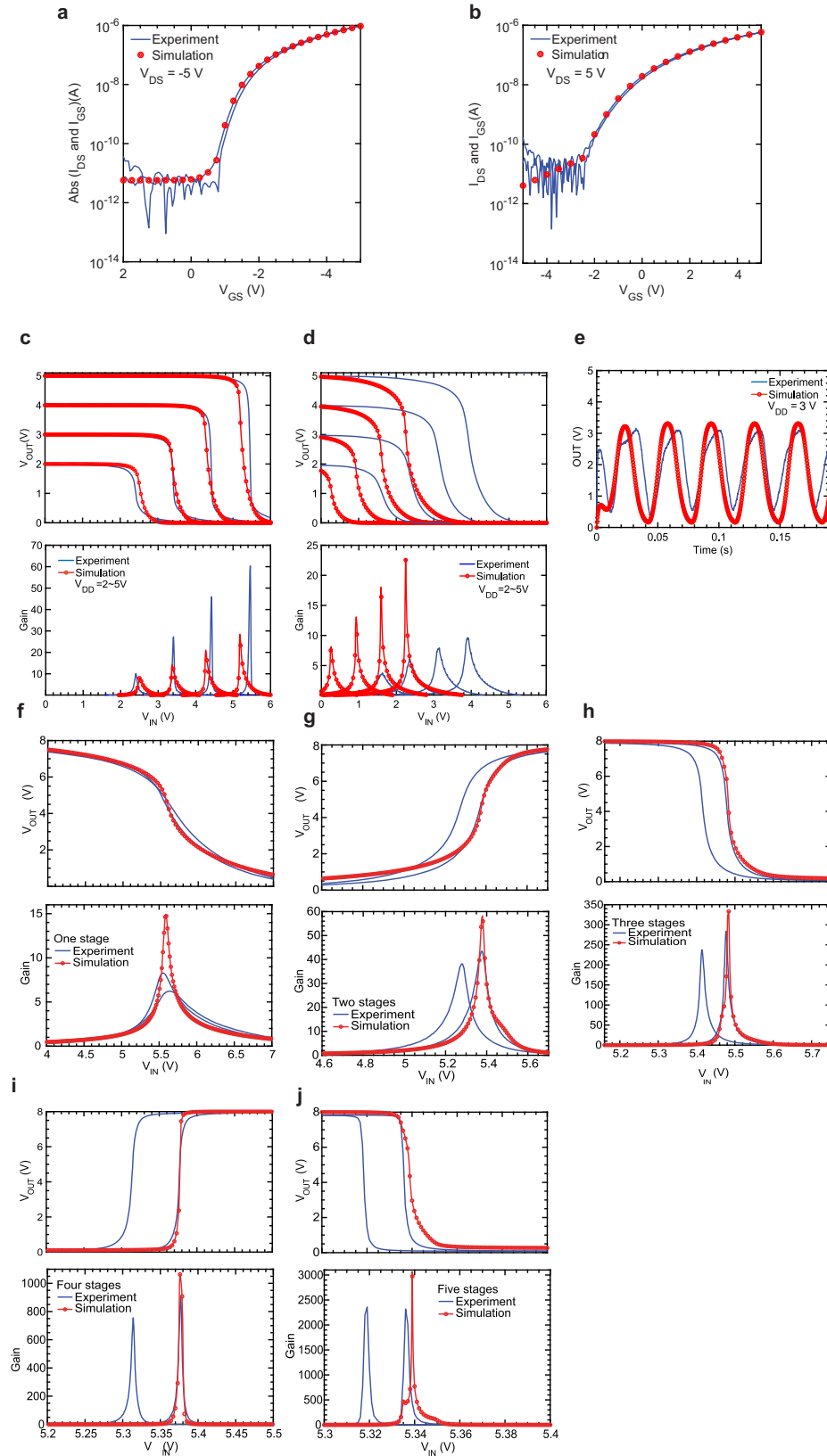
To end our discussion on simulations, it is worthwhile to clarify the difference between quasi-static and dynamic simulations. Figure 5e shows the dynamic responses of an organic ring oscillator, and the other figures are related to the quasi-static simulations of individual OFETs or oCMOS amplifiers. The dynamic simulation for the ring oscillator circuit was run by directly collecting the timed array of the output signal from the graphical interface in Matlab Simulink/Simscape. The quasi-static circuit response is measured when the circuit is assumed in a quasi-equilibrium state. The (quasi-static) transconductance curves for individual OFETs were obtained using Marinov's OFET equations considering the metal–insulator–semiconductor (MIS) tunneling (double-exponential shape) effect. The proposed quasi-static response curves of the oCMOS amplifier circuits were obtained by inputting a timed array to the input of the circuit and collecting the timed array of the circuit output signal, sweeping through the whole time domain, and comparing the output signal with the corresponding input signal at the same moment. A brief diagram to tell the difference between quasi-static and dynamic simulations is shown in Supplementary Fig. 3. Since the basic components of the circuit (OFETs and capacitors) are in the quasi-static state at each measurement moment, the quasi-static responses of the corresponding circuit were obtained when the inputs and outputs of the corresponding circuit were compared at each moment and swept through the entire time domain.

### In-vitro ECG and EMG signals amplification

To demonstrate the capability of the 270 nm amplifier, we amplify previously recorded ECG and EMG signals<sup>27</sup>, using a five-stage oCMOS amplifier. Figure 6a shows the schematic of the experimental setup consisting of a biosignal generator serving as the source of artificial EMG and ECG biosignals, a five-stage inverter, an input resistor (100 k $\Omega$ ), a capacitor (2200 nF), and the signal acquisition unit used to record the amplified signal. The resistor provides DC feedback to stabilize the circuit in the switching voltage. The input capacitor plays three roles in the circuit: (1) it prevents disturbing the operating point (switching voltage) with the noise settled on the input signal, (2) it directly affects the circuit's frequency response, and (3) it acts as an input filter<sup>22,48</sup>. Therefore, the capacitor needs to be selected according to the required monitoring frequency. The amplifier is laminated on a 125  $\mu$ m-thick PI substrate to ease the handling and expedite the characterization process. The supply voltage  $V_{DD}$  is 8 V. Given an in-vitro environment, bio-signals are simulated, applied, and finally acquired using a NI-USB 6343 data acquisition card. A Faraday cage protects the test setup from the ambient noise (e.g. power lines, lights, other equipment) increasing the signal-to-noise ratio (SNR); however, a power line noise in mV-level is still detectable in measurements. All other connectors and electrical elements are soldered together to minimize additional noise. An integrated circuit increases the fidelity of signals and suppresses the noise. However, it also significantly increases the fabrication complexity, which is beyond the scope of the current research. While such an all-integrated solution is a part of our long-term goal, here, a non-circuit-integrated capacitor and resistor are utilized to expedite the characterization and fabrication cycle.

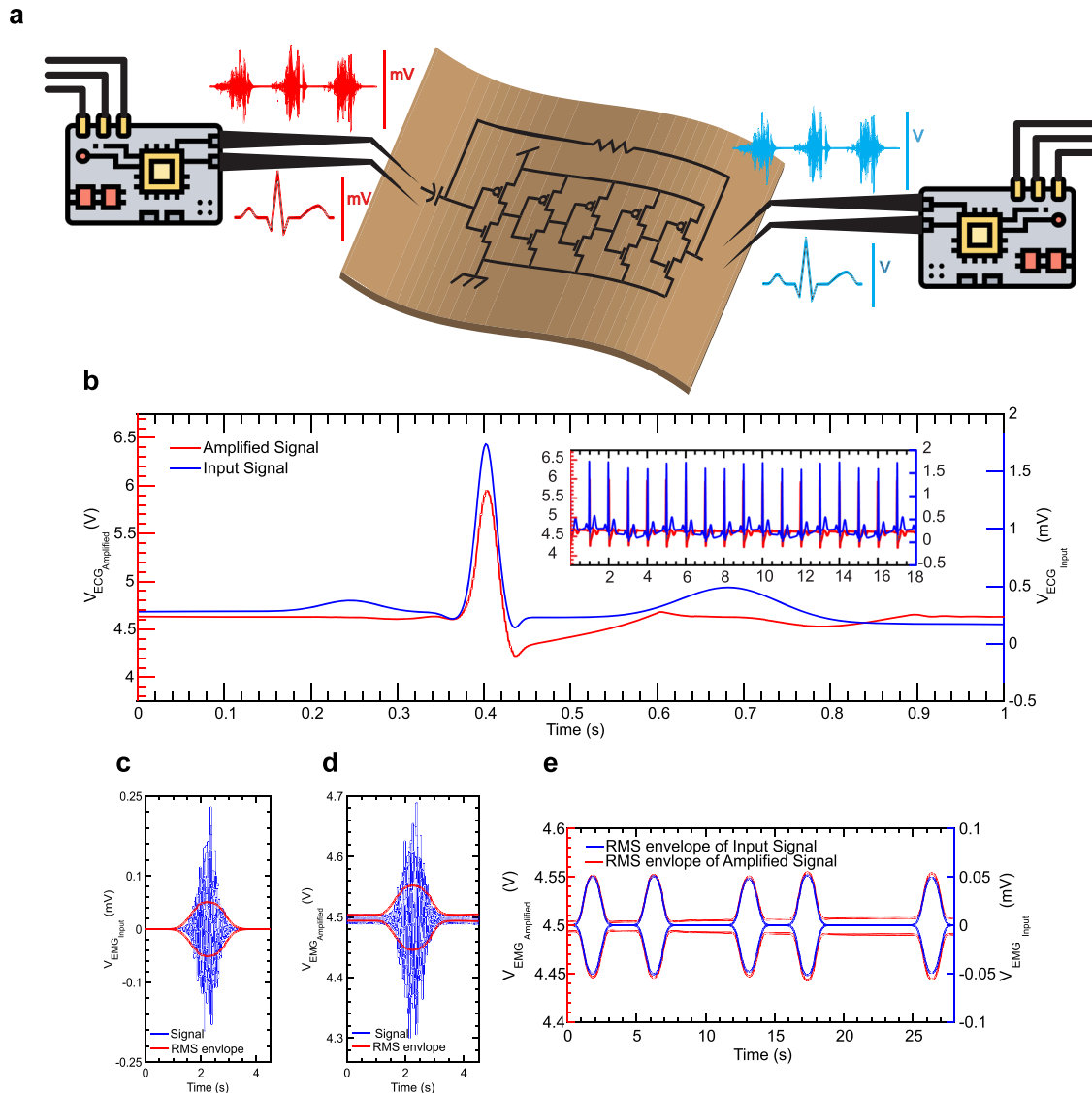
Figure 6b demonstrates the original (blue) and amplified (red) ECG signals. The peak-to-peak value of the artificial signal is 1.59 mV, and the five-stage oCMOS amplifies it with a gain that exceeds 1088, to 1.73 V. The amplification gain is less than half of the maximum reported gain (2358.19) in Table 3. The reason relies on closing the amplifier loop using the capacitor. Closing the loop affects the threshold voltage of single OFETs and intensifies the mismatch effect resulting in attenuation of the open-loop gain<sup>52</sup>. The amplifier does not reproduce the original signal precisely and distorts the signal; however, the QRS markers of the ECG signal, responsible for ventricular depolarization<sup>69</sup>, can still be extracted. Supplementary Fig. 4 shows that the intervals are preserved in the amplified signal while the original signal is distorted. The signal distortion likely occurs because of the hysteresis in the transfer characteristics function of inverters that swings within 0.11 V for one to five-stage inverters. The effect of hysteresis on signal amplification has been previously reported<sup>51</sup>. A variety of effects have been identified as causes, including trapped charge carriers at the dielectric interface. Besides, the mismatch effect due to device-to-device variability increases the distortion<sup>70,71</sup>. The inset of Fig. 6b shows the signal amplification for 18 s that exhibits the stability of the amplifier.

Figure 6c and d compare the artificial and amplified EMG signals beside the root mean square (RMS) envelope of the signals. The RMS envelope of EMG with a moving window of 1 s is deployed as an analytical tool to compare the average power of EMG signals for a given period<sup>72</sup>. The solid red lines representing the RMS envelope of signals show the same pattern for original and amplified EMG signals; however, the effect of hysteresis is trackable in the amplified signal. The artificial EMG signal's spectrum covers 20–300 Hz with a maximum peak-to-peak amplitude of 0.39 mV. The amplifier circuit increases the amplitude by a factor of 1000 (a gain of the five-stage amplifier) to 0.39 V. The amplified signal has a bias of 4.5 V, which is the switching voltage of five-stage inverters. Figure 6e illustrates the signal amplification for 28 s while the resting noise on the amplified signal has a constant frequency of 60 Hz with a maximum amplitude of 14 mV. The RMS envelope of the amplified



**Fig. 5** The simulation results. **a** The simulated characterization results of p, **b** nOFETs, **c** the pCMOS, **d** the single-stage oCMOS with  $V_{DD}$ s ranging from 2 to 5 V, and **e** the oRO comparing to experimental data, **f** the one-, **g** two-, **h** three-, **i** four-, and **j** five-stage oCMOS amplifiers.





**Fig. 6** The ECG and EMG signal amplification results using a five-stage oCMOS. **a** The measurement setup of the organic biosignal amplifier. **b** The artificial ECG signal (blue line) versus the amplified signal (red line). The inset corresponds to a period of 18 seconds of the signals. **(c)** The artificial, and **(d)** the amplified (blue lines) EMG signals comparing the RMS envelope of signals (red lines) in a period of 4.5 seconds. **(e)** The comparison of the RMS envelope of amplified (red line) and artificial (blue line) EMG signals in 28 seconds.

signals (the red line) shows a small value in resting periods resulting from amplified noise.

## DISCUSSION

We have reported 270 nm, ultra-thin, conformable, self-adhesive, and air-stable organic amplifying circuits capable of amplifying weak biosignals. We used a five-stage oCMOS architecture to amplify the signal, which exhibited a gain exceeding 1000 while preserving the time intervals of the signal. All the fabrication technologies have been reported previously<sup>26,27</sup>.

We studied the air stability and buckling effects on p and nOFETs' characteristics due to the importance of stability and flexibility in wearable devices. The results revealed that the OFETs were still working after 5 years; however, we saw a degradation in characteristics. Besides, the behavior of the devices was similar before and after buckling regardless of the thickness. We laminated OFETs on the skin to show the stability of the devices in-vivo, and the measurements showed that the ON and OFF currents started increasing over time. A 270 nm opCMOS and a

single-stage oCMOS were fabricated and characterized to amplify the signals. The opCMOS provided a high gain in the range of 64 comparing a single-stage oCMOS (10.47) at  $V_{DD}$  of 5 V; however, due to a high switching voltage close to  $V_{DD}$ s and disparities in characteristics after buckling, we selected a multi-stage oCMOS to be demonstrated as the amplifier. A 270 nm-thick oRO was fabricated and modified as a five-stage oCMOS amplifier with a maximum gain of 2358. Finally, using the five-stage CMOS amplifier, artificial ECG and EMG signals have been amplified with a gain of over 1000.

We should note that, at 300 nm, such films are too thin and always require a substrate, glass, or PI during fabrication, and for instance human skin during application. In addition, for these devices to be used in an applied environment, more robust manufacturing techniques and designs have to be implemented to make the inverters more resilient to buckling, hold their electrical integrity, and remove the hysteresis effects, as well as integrating external resistors and capacitors used here. External power sources and other measurement equipment are also needed for the OFETs and inverters to function properly. Power

applied to the system comes from a non-skin-laminated system used to prove the OFETs overall effectiveness to signal amplification but could not be implemented in a standalone system for human usage. Possible solutions for developing self-powered devices include using flexible organic photovoltaic power sources<sup>73,74</sup>, ultra-thin organic optical systems with polymer light-emitting diodes, solar cells, and photodetectors<sup>75</sup> to harvest power and provide the devices with energy. The future of ultra-thin organic biosensors relies on integrating the power supply and the circuits into a full-fledged on-skin device, giving the user independence from cable constraints and other systems that might reduce day-to-day usability.

## METHODS

### Fabrication process

The process starts with preparing FP solution by mixing 3M's Novoc 1700 and Novoc 7100 in a 1:6 volume ratio. PVA solution is achieved by dissolving PVA-205 (Kuraray Co., Ltd) in deionized water in a 1:4 weight ratio, followed by 20 min spinning at 2000 rpm and 10 min to cool and settle. The spin coating method at 1500 rpm is deployed to deposit delamination (FP) and sacrificial (PVA) layers in the air on top of a glass substrate. The deposition is followed by 5 min air drying of 80 nm layer of FP and 10 min annealing of 5  $\mu\text{m}$  PVA layer at 100 °C, respectively. Then, a 60 nm-thick layer of Parylene diX-SR is obtained from a high chemical vapor deposition (CVD) process (U-diX Coating Machine DACS-0600V-HL). A 30 nm-thick layer of Au is thermally deposited through a shadow mask at the base pressure of  $2 \times 10^{-6}$  Torr, followed by dielectric deposition (60 nm of Parylene diX-SR) using the CVD process. After dielectric deposition, the Parylene layer is thermally annealed in N<sub>2</sub>-filled glovebox for 60 min at 120 °C. The organic semiconducting layers, DN1T and N1200, the OFET's Au source, drain, and interconnections are all achieved by sequential thermal deposition using shadow masks, with the maximum rates of 0.4 and 1.5 Å s<sup>-1</sup> at the base pressure of  $2 \times 10^{-6}$  Torr, respectively, each with a thickness of 30 nm. Individual via holes are obtained using laser ablation (Keyence T-Centric SHG Laser Marker) as shown in Supplementary Fig. 5. Finally, the chip is encapsulated by 60 nm-thick layer of Parylene diX-SR. The circuits are manually delaminated from the glass substrate and laminated gently on a pre-stretched skin. After lamination, the PVA layer is removed manually by spraying deionized water and dried with N<sub>2</sub> or an air gun.

### Electrical characterization

The on-skin electrical measurement is performed after obtaining consent from the human subject. The skin is gently cleaned up using ethanol to remove organic compounds. After OFETs lamination, the electrodes are connected via electrode interconnects (details are previously outlined in ref. 27), or directly using micromanipulators, to a semiconductor parameter analyzer (HP 4155A) to characterize the device. The ECG and EMG signals are produced and collected after amplification using a data acquisition card (NI-USB 6343). The supplying voltages are also applied using NI-USB 6343. The semiconductor parameter analyzer characterizes the single devices on skin and PI film.

### DATA AVAILABILITY

Data are available upon reasonable request from the corresponding author.

### CODE AVAILABILITY

Codes for the simulation used in this study are available on GitHub (<https://github.com/yeeyoung/TCASI-ONC>).

Received: 14 March 2022; Accepted: 16 July 2023;

Published online: 11 August 2023

## REFERENCES

- Baig, M. M., GholamHosseini, H., Moqem, A. A., Mirza, F. & Lind, M. A systematic review of wearable patient monitoring systems-current challenges and opportunities for clinical adoption. *J. Med. Syst.* **41**, 115 (2017).
- Ershad, F. et al. Ultra-conformal drawn-on-skin electronics for multifunctional motion artifact-free sensing and point-of-care treatment. *Nat. Commun.* **11**, 3823 (2020).
- Kim, H. et al. Fully integrated, stretchable, wireless skin-conformal bioelectronics for continuous stress monitoring in daily life. *Adv. Sci.* **7**, 2000810 (2020).
- Li, S. et al. Physical sensors for skin-inspired electronics. *InfoMat* **2**, 184–211 (2020).
- Yao, S. et al. A wearable hydration sensor with conformal nanowire electrodes. *Adv. Healthc. Mater.* **6**, 1601159 (2017).
- Lee, H. et al. A graphene-based electrochemical device with thermoresponsive microneedles for diabetes monitoring and therapy. *Nat. Nanotechnol.* **11**, 566–572 (2016).
- Wang, X. et al. Bionic single-electrode electronic skin unit based on piezoelectric nanogenerator. *ACS Nano* **12**, 8588–8596 (2018).
- Lee, S. et al. Ultrasoft electronics to monitor dynamically pulsing cardiomyocytes. *Nat. Nanotechnol.* **14**, 156–160 (2018).
- Kabiri Ameri, S. et al. Graphene electronic tattoo sensors. *ACS Nano* **11**, 7634–7641 (2017).
- Hosseini, M. J. M. et al. Organic electronics axon-hillock neuromorphic circuit: towards biologically compatible, and physically flexible, integrate-and-fire spiking neural networks. *J. Phys. D* **54**, 104004 (2020).
- Hosseini, M. J. M., Donati, E., Indiveri, G. & Nawrocki, R. A. Organic log-domain integrator synapse. *Adv. Electron. Mater.* **8**, 2100724 (2021).
- Viola, F. A. A sub-150-nanometre-thick and ultraconformable solution-processed all-organic transistor. *Nat. Commun.* **12**, 5842 (2021).
- Ferrari, L. M., Taccola, S., Barsotti, J., Mattoli, V. & Greco, F. Ultraconformable organic devices. *Org. Flex. Electron.* **4**, 378 (2021).
- Ji, X. et al. Smart surgical catheter for c-reactive protein sensing based on an imperceptible organic transistor. *Adv. Sci.* **5**, 1701053 (2018).
- Shi, W., Guo, Y. & Liu, Y. When flexible organic field-effect transistors meet biomimetics: a prospective view of the internet of things. *Adv. Mater.* **32**, 1901493 (2020).
- Minami, T. et al. A novel ofet-based biosensor for the selective and sensitive detection of lactate levels. *Biosens. Bioelectron.* **74**, 45–48 (2015).
- Lai, S., Barbaro, M. & Bonfiglio, A. Tailoring the sensing performances of an ofet-based biosensor. *Sens. Actuators B Chem.* **233**, 314–319 (2016).
- Khodagholy, D. et al. In vivo recordings of brain activity using organic transistors. *Nat. Commun.* **4**, 1575 (2013).
- Spanu, A., Martines, L. & Bonfiglio, A. Interfacing cells with organic transistors: a review of in vitro and in vivo applications. *Lab Chip* **21**, 795–820 (2021).
- Mannsfeld, S. C. et al. Highly sensitive flexible pressure sensors with microstructured rubber dielectric layers. *Nat. Mater.* **9**, 859–864 (2010).
- Berggren, M. & Richter-Dahlfors, A. Organic bioelectronics. *Adv. Mater.* **19**, 3201–3213 (2007).
- Reuveny, A. et al. High-frequency, conformable organic amplifiers. *Adv. Mater.* **28**, 3298–3304 (2016).
- Yokota, T. et al. Sheet-type flexible organic active matrix amplifier system using pseudo-CMOS circuits with floating-gate structure. *IEEE Trans. Electron. Devices* **59**, 3434–3441 (2012).
- Sugiyama, M. et al. An ultraflexible organic differential amplifier for recording electrocardiograms. *Nat. Electron.* **2**, 351–360 (2019).
- Valov, I. & Kozicki, M. Organic memristors come of age. *Nat. Mater.* **16**, 1170–1172 (2017).
- Nawrocki, R. A., Matsuhisa, N., Yokota, T. & Someya, T. 300-nm imperceptible, ultraflexible, and biocompatible e-skin fit with tactile sensors and organic transistors. *Adv. Electron. Mater.* **2**, 1500452 (2016).
- Nawrocki, R. A. et al. Self-adhesive and ultra-conformable, sub-300 nm dry thin-film electrodes for surface monitoring of biopotentials. *Adv. Funct. Mater.* **28**, 1803279 (2018).
- Yamamoto, T. & Takimiya, K. Facile synthesis of highly  $\pi$ -extended heteroarenes, Dinaphtho[2,3-b:2',3'-f]chalcogenopheno[3,2-b]chalcogenophenes, and their application to field-effect transistors. *J. Am. Chem. Soc.* **129**, 2224–2225 (2007).
- Anderson, L., Girolamo, F. D., Barra, M., Cassinese, A. & Jacob, M. Optical properties of thermally evaporated PDI-8CN2 thin films. *Phys. Procedia* **14**, 29–33 (2011).
- Li, H., Kim, F. S., Ren, G. & Jenekhe, S. A. High-mobility n-type conjugated polymers based on electron-deficient tetraazabenzodifluoranthene diimide for organic electronics. *J. Am. Chem. Soc.* **135**, 14920–14923 (2013).

31. Melzer, C. & Seggern, H. v. Organic field-effect transistors for CMOS devices. *Org. Electron.* **223**, 189–212 (2009).
32. Mirshojaeian Hosseini, M. J. & Nawrocki, R. A. A review of the progress of thin-film transistors and their technologies for flexible electronics. *Micromachines* **12**, 655 (2021).
33. Nawrocki, R. A. Super- and ultrathin organic field-effect transistors: from flexibility to super- and ultraflexibility. *Adv. Funct. Mater.* **29**, 1906908 (2019).
34. Krebs, F. C. & Norrman, K. Analysis of the failure mechanism for a stable organic photovoltaic during 10000 h of testing. *Prog. Photovolt.* **15**, 697–712 (2007).
35. Lee, E. K., Lee, M. Y., Park, C. H., Lee, H. R. & Oh, J. H. Toward environmentally robust organic electronics: approaches and applications. *Adv. Mater.* **29**, 1703638 (2017).
36. Manceau, M., Rivaton, A., Gardette, J.-L., Guillerez, S. & Lemaître, The mechanism of photo- and thermooxidation of poly(3-hexylthiophene) (P3HT) reconsidered. *Polym. Degrad. Stab.* **94**, 898–907 (2009).
37. Guerrero, A. et al. Shelf life degradation of bulk heterojunction solar cells: Intrinsic evolution of charge transfer complex. *Adv. Energy Mater.* **5**, 1401997 (2015).
38. Yu, D., Yang, Y.-Q., Chen, Z., Tao, Y. & Liu, Y.-F. Recent progress on thin-film encapsulation technologies for organic electronic devices. *Opt. Commun.* **362**, 43–49 (2016).
39. Norrman, K., Gevorgyan, S. A. & Krebs, F. C. Water-induced degradation of polymer solar cells studied by H218O labeling. *ACS Appl. Mater. Interfaces* **1**, 102–112 (2009).
40. Guerrero, A. et al. Oxygen doping-induced photogeneration loss in P3HT:PCBM solar cells. *Sol. Energy Mater. Sol. Cells* **100**, 185–191 (2012).
41. Bulusu, A. et al. Engineering the mechanical properties of ultrabARRIER films grown by atomic layer deposition for the encapsulation of printed electronics. *J. Appl. Phys.* **118**, 085501 (2015).
42. Oh, M. H., Park, E. K., Kim, S. M., Heo, J. & Kim, H. J. Long-term stability of SiNxThin-film barriers deposited by low temperature PECVD for OLED. *ECS J. Solid State Sci. Technol.* **5**, R55–R58 (2016).
43. Kahouli, A. Effect of film thickness on structural, morphology, dielectric and electrical properties of parylene c films. *J. Appl. Phys.* **112**, 064103 (2012).
44. Afzal, T. et al. Effect of post-deposition annealing temperature on the charge carrier mobility and morphology of DPPDTT-based organic field effect transistors. *Chem. Phys. Lett.* **750**, 137507 (2020).
45. Tang, W. M., Helander, M. G., Greiner, M. T., Lu, Z. H. & Ng, W. T. Effects of annealing time on the performance of offt on glass with ZrO2 as gate dielectric. *Act. Passiv. Electron. Compon.* **2012**, 1–5 (2012).
46. Yazicioglu, R. F., Kim, S., Torfs, T., Kim, H. & Van Hoof, C. A 30  $\mu$ W analog signal processor ASIC for portable biopotential signal monitoring. *IEEE J. Solid-State Circuits* **46**, 209–223 (2011).
47. Wang, S. et al. Skin electronics from scalable fabrication of an intrinsically stretchable transistor array. *Nature* **555**, 83–88 (2018).
48. Sekitani, T. et al. Ultraflexible organic amplifier with biocompatible gel electrodes. *Nat. Commun.* **7**, 11425 (2016).
49. Sugiyama, M. et al. An ultraflexible organic differential amplifier for recording electrocardiograms. *Nat. Electron.* **2**, 351–360 (2019).
50. Fukuda, K. et al. Fully-printed high-performance organic thin-film transistors and circuitry on one-micron-thick polymer films. *Nat. Commun.* **5**, 4147 (2014).
51. Someya, T., Bao, Z. & Malliaras, G. G. The rise of plastic bioelectronics. *Nature* **540**, 379–385 (2016).
52. Lee, S. et al. Enhancement of closed-loop gain of organic amplifiers using double-gate structures. *IEEE Electron. Device Lett.* **37**, 770–773 (2016).
53. Fuketa, H. et al. 1  $\mu$ m-thickness ultra-flexible and high electrode-density surface electromyogram measurement sheet with 2V organic transistors for prosthetic hand control. *IEEE Trans. Biomed. Circuits Syst.* **8**, 824–833 (2014).
54. Lee, W. & Someya, T. Emerging trends in flexible active multielectrode arrays. *Chem. Mater.* **31**, 6347–6358 (2019).
55. Nagel, L. W. & Pederson, D. *SPICE (simulation program with integrated circuit emphasis)*. Technical Report UCB/ERL M382 (EECS Department, University of California, Berkeley, 1973).
56. Nagel, L. W. *SPICE2: A Computer Program to Simulate Semiconductor Circuits*. Ph.D. thesis, EECS Department, University of California, Berkeley (1975).
57. Liu, C. et al. A unified understanding of charge transport in organic semiconductors: the importance of attenuated delocalization for the carriers. *Mater* **4**, 608–618 (2017).
58. Matsui, H., Takeda, Y. & Tokito, S. Flexible and printed organic transistors: from materials to integrated circuits. *Org. Electron.* **75**, 105432 (2019).
59. Yang, Y., Nawrocki, R. A., Voyles, R. M. & Zhang, H. H. Modeling of the electrical characteristics of an organic field effect transistor in presence of the bending effects. *Org. Electron.* **88**, 106000 (2021).
60. Marinov, O., Deen, M. J., Zschieschang, U. & Klauk, H. Organic thin-film transistors: Part i—compact dc modeling. *IEEE Trans. Electron. Devices* **56**, 2952–2961 (2009).
61. Yang, Y., Mirshojaeian, M., Kruger, W. & Nawrocki, R. Modular modeling of organic neuromorphic circuits: toward prototyping of hardware-level spiking neural networks. *IEEE Trans. Circuits Syst. I Regul. Pap.* **70**, 1161–1174 (2023).
62. Liao, C.-S. & Hwu, J.-G. Subthreshold swing reduction by double exponential control mechanism in an MOS gated-MIS tunnel transistor. *IEEE Trans. Electron. Devices* **62**, 2061–2065 (2015).
63. Green, M., King, F. & Shewchun, J. Minority carrier MIS tunnel diodes and their application to electron- and photo-voltaic energy conversion—I. Theory. *Solid State Electron.* **17**, 551–561 (1974).
64. Abadias, G. et al. Review article: stress in thin films and coatings: Current status, challenges, and prospects. *J. Vac. Sci.* **36**, 020801 (2018).
65. Gunda, M., Kumar, P. & Katiyar, M. Review of mechanical characterization techniques for thin films used in flexible electronics. *Crit. Rev. Solid State Mater. Sci.* **42**, 129–152 (2016).
66. Yang, Y. et al. Fractional drift-diffusion model of organic field effect transistors including effects of bending stress for smart materials. In *ASME 2021 Conference on Smart Materials, Adaptive Structures and Intelligent Systems of Smart Materials, Adaptive Structures and Intelligent Systems*. Paper no.: SMASIS2021-68344, V001T02A013; 8 pp. <https://doi.org/10.1115/SMASIS2021-68344>.
67. Yang, Y., Nawrocki, R. A., Voyles, R. M. & Zhang, H. H. A fractional drift diffusion model for organic semiconductor devices. *Comput. Mater. Contin.* **69**, 237–266 (2021).
68. Heidari, H., Wacker, N. & Dahiya, R. Bending induced electrical response variations in ultra-thin flexible chips and device modeling. *Appl. Phys. Rev.* **4**, 031101 (2017).
69. Yazicioğlu, R. F., Hoof, C. V. & Puers, R. *Biopotential Readout Circuits for Portable Acquisition Systems. Analog Circuits Signal Process.* (eds Ismail, M. & Sawan, M.) (Springer Science, 2008).
70. Lee, S. et al. Enhancement of closed-loop gain of organic amplifiers using double-gate structures. *IEEE Electron Device Lett.* **37**, 770–773 (2016).
71. Kaushik, B. K., Kumar, B., Negi, Y. S. & Mittal, P. Prospects and limitations of organic thin film transistors (OTFTS). *Adv. Intell. Syst. Comput.* 125–139 (2012).
72. Mark Burden, A., Lewis, S. E. & Willcox, E. The effect of manipulating root mean square window length and overlap on reliability, inter-individual variability, statistical significance and clinical relevance of electromyograms. *Man. Ther.* **19**, 595–601 (2014).
73. Park, S. et al. Self-powered ultra-flexible electronics via nano-grating-patterned organic photovoltaics. *Nature* **561**, 516–521 (2018).
74. Yu, K. et al. Organic photovoltaics: toward self-powered wearable electronics. *Proc. IEEE* **107**, 2137–2154 (2019).
75. Jinno, H. et al. Self-powered ultraflexible photonic skin for continuous bio-signal detection via air-operation-stable polymer light-emitting diodes. *Nat. Commun.* **12**, 2234 (2021).

## ACKNOWLEDGEMENTS

This work was partially supported by the Japanese Society for the Promotion of Science (Grant No. 15F15062), Office of Naval Research Young Investigator Program, Award No. N00014-21-1-2585, and Purdue Polytechnic Institute's graduate fellowship. The authors would also like to acknowledge the help of Prof. Walter Daniel Leon-Salas from Purdue University for his help in device characterization and fruitful discussions, and Yanyang Ju from The University of Tokyo for her help in demonstrating the on-skin lamination of our electronic skin.

## AUTHOR CONTRIBUTIONS

R.A.N. conceived the research. R.A.N. performed device fabrication with help from T.Y. and S.L. M.J.M.H., W.K., and R.A.N. each contributed to data collection. Y.Y., M.J.M.H., and W.K. all helped in conceiving and deploying the simulation environment. R.A.N. and T.S. obtained the funding. M.J.M.H. and Y.Y. wrote the manuscript, including the figures, with major edits from R.A.N. and comments from T.Y. and S.L.

## COMPETING INTERESTS

The authors declare no competing interests.

## ADDITIONAL INFORMATION

**Supplementary information** The online version contains supplementary material available at <https://doi.org/10.1038/s41528-023-00267-y>.

**Correspondence** and requests for materials should be addressed to Robert A. Nawrocki.

**Reprints and permission information** is available at <http://www.nature.com/reprints>

**Publisher's note** Springer Nature remains neutral with regard to jurisdictional claims in published maps and institutional affiliations.



**Open Access** This article is licensed under a Creative Commons Attribution 4.0 International License, which permits use, sharing, adaptation, distribution and reproduction in any medium or format, as long as you give appropriate credit to the original author(s) and the source, provide a link to the Creative Commons license, and indicate if changes were made. The images or other third party material in this article are included in the article's Creative Commons license, unless indicated otherwise in a credit line to the material. If material is not included in the article's Creative Commons license and your intended use is not permitted by statutory regulation or exceeds the permitted use, you will need to obtain permission directly from the copyright holder. To view a copy of this license, visit <http://creativecommons.org/licenses/by/4.0/>.

© The Author(s) 2023